https://doi.org/10.5194/egusphere-2025-5121
Preprint. Discussion started: 7 April 2026

Optimization of the Fast Layer Transmittance Algorithm in RTTOV v13.1 for Strong Water Vapor Absorption Channels of the FY-3F HIRAS-II Instrument Using LBLRTM v12.11

Panxiang Zhang[1,5], Peng Zhang[2*], Gang Ma[3*], Rui Li[1], Lu Lee[4], Wenguang Bai[4], Chengli Qi[4]

[1]University of Science and Technology of China, Hefei, 230052, China
[2]Meteorological Observation Centre of CMA, Beijing, 100081, China
[3]China Meteorological Administration Earth System Numerical Prediction Centre, Beijing, 100081, China
[4]National Satellite Meteorological Centre, Beijing, 100081, China
[5]Beijing Huayun Shinetek technology Co., Ltd., Beijing, 100081, China

Correspondence to: Peng Zhang (zhangp@cma.gov.cn), Gang Ma (magang@cma.gov.cn)

Abstract

Fast and accurate calculation of atmospheric transmittance is essential for infrared atmospheric remote sensing and satellite data assimilation. However, fast radiative transfer models show significant errors in strong water vapour absorption channels (e.g., near 6.7 μm). An important reason is that the numerical instability encountered during the regression of transmittance coefficients when dealing with lower and middle atmosphere. To address this, this study proposes an optimized scheme to calculate atmospheric transmittance vertical profiles for the RTTOV (Radiative Transfer for TOVS) fast transmittance algorithm. The method introduces a physically motivated transmittance threshold to sub-select training samples and employs cumulative transmittance-based weighting factor within a weighted least squares regression to recalibrate the transmittance coefficients. It aims to optimize the calculation scheme for transmittance coefficients of the Hyperspectral Infrared Atmospheric Sounder-II (HIRAS-II) instrument onboard Fengyun 3F satellite (FY-3F). The method is assessed by calculations on the training profile datasets provided within the RTTOV model framework. By comparing transmittance and brightness temperature calculations at 6.7 microns from this method with those from a line-by-line model and observations from HIRAS-II, the results show that the accuracy of the forward model for the 6.7 μm absorption channel is significantly enhanced by applying a threshold-based noise reduction method. This improvement enhances the stability and reliability of the transmittance calculations for this strong absorption band. Further accuracy enhancements are obtained by incorporating weighting corrections into the calculations of transmittance coefficients. The root mean square error (RMSE) and bias of the observation minus background (OMB) time series for FY-3F HIRAS-II demonstrate that the transmittance coefficient calculation scheme with weighting factor correction improves the forward model accuracy, which is more consistent with RTTOV simulation results. The OMB bias at the 6.7 μm absorption peak channel performs better than that of RTTOV, while the OMB bias on both sides of the 6.7 μm absorption peak channel remains consistent with RTTOV.

1 Introduction

The Hyperspectral Infrared Atmospheric Sounder (HIRAS; Li et al., 2022; Zhou et al., 2025) is a key instrument onboard the FengYun-3 (FY-3) polar-orbiting meteorological satellite series, specifically FY-3D (Zhang et al., 2018), and the 2nd

https://doi.org/10.5194/egusphere-2025-5121
Preprint. Discussion started: 7 April 2026

generation HIRAS-II instrument on FY-3E (Zhang et al., 2024) and FY-3F (Zeng et al.,2025). The first-generation HIRAS instrument onboard FY-3D covers three spectral bands: long-wave infrared (LW) from 648.75 to 1136.25 cm^{-1} (15.41 to 8.8 μm), medium-wave infrared (MW) from 1208.75 to 1751.25 cm^{-1} (8.27 to 5.71 μm), and short-wave infrared (SW) from 2153.75 to 2551.25 cm^{-1} (4.64 to 3.92 μm), with a nadir spatial resolution of 16 km (Wu et al., 2020). In contrast, the second-generation HIRAS-II instrument on FY-3E and FY-3F offers expanded spectral coverage: the LW band extends to 1169.375 cm^{-1}, the MW band spans 1167.5 to 1921.25 cm^{-1} (8.57 to 5.2 μm), and the SW band starts from 1919.375 cm^{-1}, while maintaining 0.625 cm^{-1} spectral resolution and improving nadir resolution to 14 km (Zeng et al.,2025). This instrument is primarily used to retrieve high-precision vertical profiles of atmospheric temperature, humidity, ozone, and atmospheric composition variables, from the Earth's surface to the lower stratosphere (Alvarado et al., 2013, Menzel et al., 2018; Zhou et al., 2025). Retrieval of such profiles from hyperspectral infrared remote sensing data typically adopts the one-dimensional variational (1D-VAR) technique, and the performance of this retrieval algorithm is highly dependent on the simulation accuracy of the radiative transfer forward model (Zhu et al., 2020; Li et al.,2022). High-resolution infrared atmospheric sounding data has been assimilated into global Numerical Weather Prediction Models (NWP) by organizations such as the European Centre for Medium-Range Weather Forecasts (ECMWF), making it one of the most influential satellite observations for improving numerical forecast quality (Eyre et al., 2020; Eyre et al., 2022). Fast radiative transfer models establish functional relationships between atmospheric state variables in numerical weather prediction models and satellite channel radiances (Bai et al., 2017; Bai et al., 2020). Therefore, both aspects must be scrutinized to ensure the accuracy of the fast radiative transfer model in the assimilation of satellite observations (Eyre et al., 1993; Matricardi et al., 2004).

Although line-by-line radiative transfer models, such as the Line-by-line Radiative Transfer Model (LBLRTM; Clough et al., 2005) by Atmospheric and Environmental Research and the Reference Forward Model (RFM; Dhudia, 2017), exhibit high computational accuracy, the high computational cost make it difficult to apply in operational numerical weather forecasting and retrievals (Mcmillin and Fleming, 1976; Matricardi and Saunders, 1999; Saunders et al., 1999). Fast radiative transfer models convert layer-by-layer atmospheric transmittance coefficients into linear polynomial approximations. This approach improves computational efficiency, enabling forward models to be applied in assimilation and inversion operations (Mcmillin et al., 1995; Li et al., 2017; Schmit et al., 2019). By assuming atmospheric state variables and the radiative spectral characteristics of spaceborne sensor channels exhibit no linear correlation, the accurate expression for layer-by-layer monochromatic atmospheric transmittance can be simplified to a channel-independent multivariate linear expression. The least-squares solution to the system of equations constructed from this multivariate linear expression yields the fast forward model coefficients for the transmittance of each channel. These coefficients are multiplied by the predictors derived from atmospheric sample profiles in turn and then summed, which produces the layer transmittance for each channel (Hannon et al., 1996; Kleespies et al., 2004; Chevallier et al., 2006). When atmospheric sample profiles are representative, the fast radiative transfer model can be applied universally (Matricardi, 2003).

The fast radiative transfer model was first proposed by McMillin and Fleming (1976), based on a Taylor series expansion. It uses statistical regression methods to calculate satellite channel transmittance within fixed gas absorption layers, evolving into

https://doi.org/10.5194/egusphere-2025-5121
Preprint. Discussion started: 7 April 2026

the first fast radiative transfer model for satellite forward model: Optical Path Transmittance Model (OPTRAN). Subsequently, this model was applied to the Community Radiative Transfer Model (CRTM). Since variations in ozone content significantly affect simulations for channels near 9.6μm and 118GHz, O_3 is separated from fixed gases, and treated as a variable gas for independent calculation (Eyre and Woolf, 1988). This approach later evolved into the RTTOV radiative transfer model. Applying water vapor and ozone as variable gases in the fast transmittance calculation for the infrared and microwave detectors at the European Centre for Medium-Range Weather Forecasts, although the simulation errors in the stratosphere, surface, water vapor, and ozone absorption channels exceed instrument noise, this method remains applicable to numerical weather prediction data assimilation systems (Saunders et al., 1999; Matricardi et al., 2004). Using line-by-line models to calculate transmittance as the true value, a fast transmittance calculation model for infrared hyperspectral vertical detectors was developed. This model was used to preform pre-launch simulation studies of the IASI instrument. Results indicate that the simulated brightness temperature difference between the IASI fast radiative transfer model and the line-by-line model is smaller than the instrument noise (Matricardi and Saunders, 1999; Matricardi, 2007; Matricardi and Mcnally, 2008). Subsequently, a high-resolution transmittance database was generated using 83 atmospheric sample profiles (2016) and LBLRTM v12.11, thereby enhancing the accuracy of the forward model for satellite infrared detectors (Matricardi, 2008; Matricardi and Mcnally, 2008). Di et al. (2018) proposed a weighted least squares method, incorporating local sample profiles alongside the 83 atmospheric sample profiles, to construct a fast transmittance model for FY-4A GIIRS. Compared to line-by-line radiative transfer model simulations of brightness temperatures, the root mean square error was less than 0.4K. Bormann et al. (2009) and Hocking et al. (2021) successively introduced new parameterization schemes in RTTOV to calculate trace gas channel transmittances, further improving the simulation accuracy of trace gas absorption channels. With the advancement of fast radiative transfer models, the main models currently used are RTTOV (Radiative Transfer for TOVS), developed by the European Centre for Medium-Range Weather Forecasts (Hocking et al., 2021), CRTM (Community Radiative Transfer Model), developed by the U.S. Satellite Data Simulation Joint Center (Johnson et al., 2023), and ARMS (Advanced Radiative Transfer Modeling System), developed by the China Meteorological Administration (Weng et al., 2020).

As a key factor influencing weather and climate, water vapor is essential for cloud formation and precipitation. However, existing fast radiative transfer models have been shown to exhibit significant biases in simulating radiances within strong water vapor absorption bands (Saunders et al., 1999; Matricardi et al., 2004; Saunders et al., 2018). These errors directly propagate into retrieved atmospheric profiles, degrading the accuracy of downstream applications such as numerical weather prediction. Saunders et al. (2018) noted that for satellite detection channels affected by water vapor, the error is greater than that of window channels, indicating that the simulation accuracy of fast radiative transfer models still needs improvement. Improving the simulation accuracy of water vapor absorption channels in radiative transfer models is crucial for the effective use of satellite infrared data in numerical forecasting and climate analysis.

To further reduce simulation errors in Hyperspectral Infrared Atmospheric Sounder (HIRAS; Li et al., 2022; Zhou et al., 2025) and advance its application in numerical weather prediction, this study addresses the significant simulation brightness temperature errors in the water vapor absorption channels of infrared hyperspectral vertical sounders (Saunders et al., 2018).

https://doi.org/10.5194/egusphere-2025-5121
Preprint. Discussion started: 7 April 2026

We optimized the channel transmittance coefficient calculation model for the FY-3F HIRAS-II (Zhou et al., 2025) instrument by applying a thresholding method to exclude poor-quality samples and introducing different weights as constraints. These modifications significantly improved the forward model accuracy in the 1300~1600 cm^{-1} water vapor absorption band. The optimization is developed and evaluated using LBLRTM v12.11 on the standard RTTOV atmospheric profile datasets. Applied to the strong water vapour channels of the FY-3F HIRAS-II instrument, the optimized scheme significantly reduces errors in simulated transmittance compared to the baseline RTTOV v13.1 algorithm. Validation against HIRAS-II observations shows a notable improvement.

From an application perspective, the optimized model not only significantly enhances the reliability of fast radiative transfer models but also provides strong technical support for improving the quality of HIRAS-II satellite data assimilation, and the accuracy of middle and lower atmospheric water vapor retrieval, which is of great significance for deepening the understanding of the water cycle process, monitoring climate change, and improving the level of atmospheric environmental governance. It should be noted that this study focuses on the 6.7 μm channel of HIRAS-II, but the optimization scheme can be extended to the fast transmittance calculation for strong absorption channels of other trace gases (e.g., carbon dioxide and ozone) in satellite remote sensing. Sect. 2 details the experimental methodology for establishing the profile lookup table and weighting function, as well as the data employed. Sect. 3 outlines the experimental design, Sect. 4 presents an analysis of experimental results, and Sect. 5 covers the results and discussion.

2 Theory and Methods

2.1 Fast Radiative Transfer Model

RTTOV was first developed as a fast radiative transfer model at the European Centre for Medium-Range Weather Forecasts (ECMWF) in the early 1990s (Eyre, 1991, 1993). The original fast radiative transfer model (RTTOV-3) described by Eyre (1991). After the mid-1990s, development was continued by the Numerical Weather Prediction Satellite Application Facility (NWP SAF; Rayer, 1995), supported by the European Organisation for the Exploitation of Meteorological Satellites (EUMETSAT). Subsequently, starting with RTTOV-6 in March 2000, the NWP SAF made the technical documents for this fast radiative transfer model publicly available via its official website (Saunders et al., 2000). The current version, RTTOV14 (Hocking et al., 2025), supports fast radiative transfer calculations for over 120 satellite sensors covering the visible, near-infrared, infrared, microwave, and ultraviolet.

In the RTTOV model, infrared spectral gas absorption is primarily caused by water vapor, ozone, and a uniformly mixed gas with a nearly constant spatial and temporal distribution. The total channel transmittance is calculated as the product of the transmittances of these three components (as shown in Eq. (1)). Eq. (1) accounts for the absorption overlap among these gases, thereby reducing its adverse effect on the forward model's accuracy.

https://doi.org/10.5194/egusphere-2025-5121
Preprint. Discussion started: 7 April 2026

$$\tau_{i,j}^{total} = \tau_{i,j}^{mix} * \frac{\tau_{i,j}^{mix+wv}}{\tau_{i,j}^{mix}} * \frac{\tau_{i,j}^{mix+wv+o_3}}{\tau_{i,j}^{mix+wv}} \quad (1)$$

The relationship between channel transmittance and optical thickness is defined by Eq. (2). The optical depth for a given atmospheric layer is calculated using the iterative Eq. (3):

$$d_{i,j} = -ln(\tau_{i,j}) \quad (2)$$

$$d_{i,j} - d_{i,j-1} = -ln\left(\frac{\tau_{i,j}}{\tau_{i,j-1}}\right) = \sum_{k=1}^{n} a_{i,j,k} X_{k,j} \quad (3)$$

where $X_{k,j}$ is the predictor, which is a function of zenith angle, temperature, humidity, and pressure. $d_{i,j}$ denotes the optical thickness from atmospheric level j to the top of the atmosphere for i channel, and $\tau_{i,j}$ represents the transmittance from level j to the top of the atmosphere. $a_{i,j,k}$ is the transmittance coefficient, where i denotes the channel index, j denotes the pressure level index, and k denotes the predictor index. For selected atmospheric sample profiles, we use the LBLRTM to compute an accurate channel-by-channel transmittance dataset. When the left-hand side of Eq. (3) and the transmittance predictors known, Eq. (3) forms an overdetermined homogeneous linear system of equations: $a_{i,j,k}$ is the least-squares solution to this system.

2.2 A Threshold Approach

The training dataset comprises 83 atmospheric profiles. While these profiles cover a wide range of extreme meteorological conditions (Chevallier et al., 2006), not every individual profile is utilized in the layer-by-layer training of the fast transmittance coefficients. Based on the instrument characteristics of the High-Resolution Infrared Spectrometer for Atmospheric Vertical Sounding, the spectral response function is constructed using the Hamming window function (Harris et al., 1987). Because the values of the two wings of the spectral response function (SRF) of interferometric instruments oscillate around zero, the shape of this function can lead to physically unrealistic negative transmittance values in strong absorption bands after convolution with the monochromatic spectrum (transmittance is close to zero). Additionally, for strong water vapor absorption channels, under conditions of abundant water vapor content, the total transmittance from a given level to the top of the atmosphere (TOA) becomes an extremely small quantity in the middle and lower atmosphere. Thus, division by small quantities ($\frac{\tau_{i,j}}{\tau_{i,j-1}}$) arises when calculating the optical depth of this layer. This leads to abnormal values in the total transmittance, causing instability in solving the least-squares solution for the system of Eq. (3). Setting strict thresholds can eliminate poorly profiles, improving the stability of the least-squares solution. However, the choice of thresholds significantly affects both the training profiles and the optimality of the least-squares solution. The threshold method sets distinct thresholds for different channels to select atmospheric profiles for the regression. when the level-to-space transmittance falls below this threshold, samples from below that height (i.e., at higher pressure/lower altitude) are considered too strongly affected by computational errors and are therefore excluded. Since the magnitude of transmittance is relatively small below that height (i.e., at higher pressure/lower altitude), the transmittance from this layer to the surface layer is considered to make a negligible contribution to the atmosphere.

https://doi.org/10.5194/egusphere-2025-5121
Preprint. Discussion started: 7 April 2026

2.3 The Weighted Least-Squares Method

Ordinary least squares (OLS) obtains the optimal solution to the objective function when the sum of squared deviations between actual and predicted values is minimized. It is defined as:

$$S = \sum_{m=1}^{m=p}(y_m - \hat{y}_m)^2 \quad (m = 1,2,3, \dots \dots, p) \tag{4}$$

Where $y = d_j - d_{j-1}$, j denotes the level number from 1 to 101 levels, y_m denotes the true values of the m-th sample, i.e., the optical depth of a given layer derived from line-by-line radiative transfer models, and $\hat{y}_m$ denotes the fitted values of the m-th sample, i.e., the optical depth of each layer obtained using the least squares solution. Where m denotes the index of the training profiles involved in the statistical analysis from 1 to 83*6, and p denotes the total number of samples in the training dataset. S denotes the sum of squared deviations between actual and predicted values. when S is minimized, the objective function $\hat{y}_m$ obtains the optimal solution.

The ordinary least squares method assumes homoscedasticity, giving equal weight to all data involved in the calculation. However, in practice, some data are more important than others. To ensure the number of samples involved in the calculation while reducing the contribution of non-critical data, a method of assigning different weights to the data is adopted. Weighted least squares method enables models to better fit datasets with heteroscedastic properties by assigning different weights to various data. In this case, eq. (4) becomes:

$$S = \sum_{m=1}^{p} W_m(y_m - \hat{y}_m)^2 \ (m = 1,2,3, \dots \dots, p) \tag{5}$$

where W_m represents the weight factor. For a given sample profile, During the process, the weight factor W_m are iteratively updated until the optimal solution $\hat{y}$ is obtained. Therefore, after introducing weight factor into the fast transmittance calculation model for a given channel, the homogeneous linear equation Eq. (3) can be transformed as follows:

$$d_j - d_{j-1} = \ W_j \sum_{k=1}^{K} a_{j-1,k} X_{k,j-1} \quad (j = 2 \ to \ n), W_j = \sqrt{\tau_j \cdot \tau_j} \tag{6}$$

Where j denotes the level number from 2 to n levels, k denotes the predictors number from 1 to K, d_j denotes the sum of optical depth from level j to space, $d_j - \ d_{j-1}$ denotes optical depth for layer $j-1$, $X_{k,j-1}$ are the predictors for $j-1$ levels and k predictors, and $a_{j-1,k}$ are the coefficients for $j-1$ levels and k predictors. τ_j denotes transmittance from level j to space, the absolute value of the transmittance τ_j is the weight factor W_j for layer $j-1$.

The second weighting scheme involves applying weights to both the left-hand side term, $d_j - d_{j-1}$ and the right-hand side term $X_{k,j}$, before solving the system of equations, as shown in Eq. (7) and (8)

$$X'_{k,j-1} = W_j X_{k,j-1} \tag{7}$$

$$(d_j - d_{j-1})' = W_j(d_j - d_{j-1}) \tag{8}$$

the weight factor expression is $W_j = \sqrt{\tau_j \cdot \tau_j}$. Eq. (3) is transformed into Eq. (9):

$$\left(d_j - d_{j-1}\right)' = \left(-ln\left(\tau_j/\tau_{j-1}\right)\right)' = \sum_{k=1}^{K} a_{j,k} X'_{k,j} \tag{9}$$

https://doi.org/10.5194/egusphere-2025-5121
Preprint. Discussion started: 7 April 2026

3 Experimental Design

3.1 Experimental Scheme

This study optimizes the transmittance coefficient for the HIRAS-II 6.7 μm water vapor absorption channel (Matricardi and Saunders, 1999; Matricardi, 2007) using two methods: atmospheric profile selection and a weighted least-squares algorithm. We evaluate the forward model by comparing its output with both line-by-line radiative transfer model (LBLRTM) simulations and actual HIRAS-II observations. LBLRTM v12.11 by Atmospheric and Environmental Research, Inc. (AER) is used to compute monochromatic transmittances from 650 to 2600 cm^{-1} (3.8 to 15.4 microns) at a 0.001 cm^{-1} spectral resolution for 83 profile training datasets. The calculations cover 101 pressure levels (from 1100 to 0.005 hPa) and six zenith angles, accounting for refractive effects. They include absorption by a uniform mixture of 26 gases (CO_2, N_2O, CO, CH_4, O_2, NO, SO_2, NO_2, NH_3, HNO_3, OH, HF, HCl, HBr, HI, ClO, OCS, H_2CO, HOCl, N_2, HCN, CH_3Cl, H_2O_2, C_2H_2, C_2H_6, PH_3), water vapor (line and continuum), and ozone. These high-resolution transmittances are then convolved with the HIRAS-II spectral response function using Eq. (12) to produce the "true" transmittance values.

We calculated fast transmittance coefficients for the HIRAS mid-wave channels within the RTTOV framework using the RTTOV v7 predictors (Saunders et al., 2018). To evaluate the impact of the threshold method and weighted least squares on forward model accuracy, we selected channels representing different atmospheric layers. These include the 6.7 μm absorption peak (Channel 1372, central wavenumber 1506.875 cm^{-1}), mid-level (channel 1239, central wavenumber 1423.75 cm^{-1}; channel 1596, central wavenumber 1646.875 cm^{-1}) and lower-level (channel 1169, central wavenumber 1380 cm^{-1}; channel 1729, central wavenumber 1730 cm^{-1}) atmospheric observation channels at the left and right ends of the peak region were selected to analyze the effects of the threshold method and weighted least squares on forward model accuracy, respectively.

We calculated fast transmittance coefficients for the HIRAS mid-wave channels within the RTTOV framework using the RTTOV v7 predictors (Saunders et al., 2018). To evaluate the impact of the threshold method and weighted least squares on forward model accuracy, we selected channels representing different atmospheric layers. These include the 6.7 μm absorption peak (Channel 1372, 1506.875 cm^{-1}) and two mid-level channels (Channels 1239 and 1596 at 1423.75 cm^{-1} and 1646.875 cm^{-1}, respectively) and two lower-level channels (Channels 1169 and 1729 at 1380 cm^{-1} and 1730 cm^{-1}, respectively) located on either side of the peak.

We analyze the impact of the threshold and weighted least-squares methods on forward model accuracy according to the experimental design in Table 1. Based on the 1976 U.S. standard atmospheric profile, we employ the RTTOV radiative transfer model to analyze mid-wave spectrum simulations of brightness temperature and calculate the height of the weighting function for selected channels (as shown in Fig. 4). The weighting function is calculated using Eq. (10):

Using the 1976 U.S. Standard Atmosphere, we employ the RTTOV model to simulate mid-wave brightness temperatures and compute the weighting function peaks for the selected channels (Fig. 1). The weighting function is calculated using

$$WF = \frac{\partial \tau}{\partial \ln P} \tag{10}$$

https://doi.org/10.5194/egusphere-2025-5121
Preprint. Discussion started: 7 April 2026

Where WF denotes the weighting function, τ represents the channel transmittance, and P indicates atmospheric pressure. As shown in Fig. 1, the weighting function peak indicates the atmospheric altitude sensed by the channel.

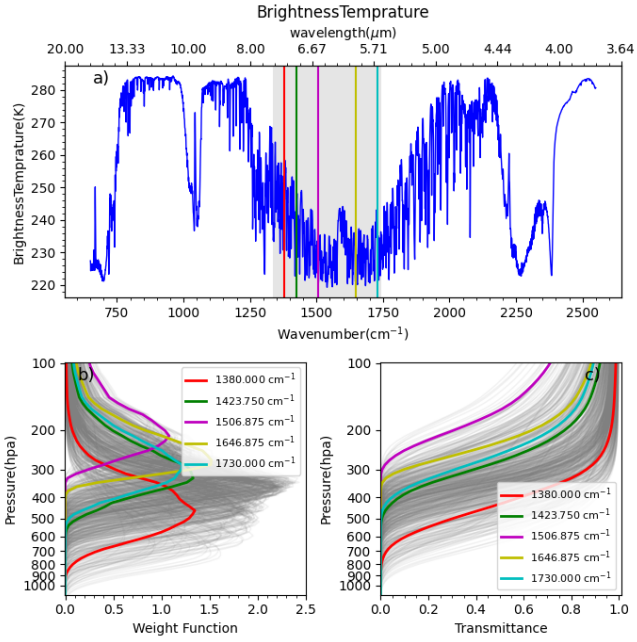

Figure 1: Distribution of Simulated Brightness Temperature and Weighting Functions for HIRAS-II Channels

Table 1. Experimental Design

Experimental Scheme Abbreviation	Remarks Content
LSM0	The model utilizes an unconstrained ordinary least squares regression on all data points to determine the channel transmittance coefficients.
LSM1	Ordinary least squares (OLS) is employed to determine the channel transmittance coefficients. A thresholding method is used to select the atmospheric profiles.
LSM2	Channel transmittance coefficients are derived using weighted ordinary least squares, with atmospheric profiles selected through a thresholding method.
LSM3	Atmospheric profiles are selected through a thresholding method, followed by the application of weights to the selected samples. The channel transmittance coefficients are subsequently obtained using an ordinary least squares solution.

The validation against HIRAS observations is conducted over the 60°S~60°N region. We use ERA5 global profiles of temperature and humidity as the input to RTTOV v13.2. For surface emissivity, the IREMIS scheme is applied over sea, and the CAMEL climatology atlas scheme over land. The optimized transmittance coefficients are then used to simulate clear-sky brightness temperatures for the FY-3F HIRAS-II channels at 1380 cm^{-1}, 1506.875 cm^{-1}, and 1646.875 cm^{-1}. The model simulations were evaluated against clear-sky satellite observations.

https://doi.org/10.5194/egusphere-2025-5121
Preprint. Discussion started: 7 April 2026

3.2 Experimental Data

This study uses 83 profile training datasets from Matricardi (2008), which are widely adopted for training fast transmittance coefficients in radiative transfer models, including RTTOV, CRTM, and ARMS. These profiles provide global coverage of temperature, water vapor, and ozone across 101 pressure levels (1100 to 0.005 hPa). They represent a range of atmospheric conditions, including seasonal extremes. Temperature ranges from a minimum of 159.62 K to a maximum of 318.26 K. The spatial distribution of the profiles is shown in Fig. 1(a), while the vertical distribution characteristics of temperature and humidity profiles are depicted in Fig. 1(b) and (c), respectively.

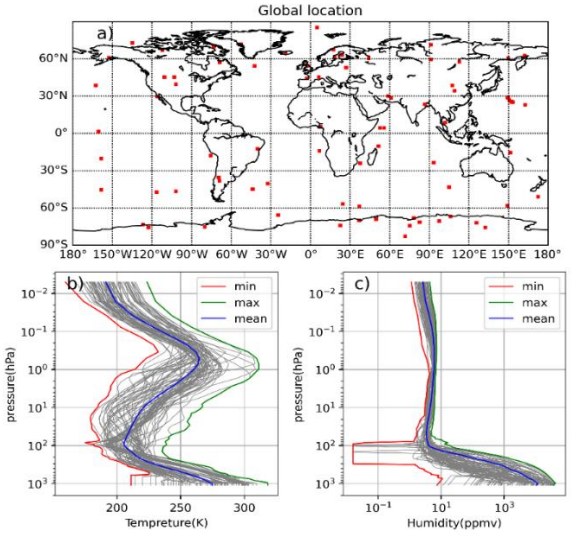

Figure 2: (a) Geographic locations of the 80 profiles used for coefficient training, which cover diverse surface types, latitudes, and meteorological conditions. (b) and (c) Show the vertical distributions of 83 temperature and humidity profiles.

The High-Resolution Infrared Spectrometer for Atmospheric Vertical Sounding (HIRAS-II) has a spectral coverage of 650~2550 cm^{-1} (3.8 to 15.4 microns) using continuous spectral scanning with a spectral resolution of 0.625 cm^{-1}. Three bands cover the 15 μm CO_2 band (LW: 648.75~1169.375 cm^{-1}), the 6.7 μm H_2O band (MW: 1167.5~1921.25 cm^{-1}), and the 4.3 μm CO_2 band (SW: 1919.375~2551.25 cm^{-1}), totaling 3053 channels (http://www.nsmc.org.cn/nsmc/cn/instrument/HIRAS-2.html). Satellite observation data were obtained from the Fengyun Satellite Remote Sensing Data Service Network (http://data.nsmc.org.cn/DataPortal/cn/home/index.html). FY-3F HIRAS-II L1 observation data from August 2024 and February 2025 were selected to represent summer and winter, respectively.

3.3 Data Preprocessing

3.3.1 Apodization of HIRAS-II data

HIRAS-II is a Michelson interferometer that measures interference patterns of incoming radiation. This pattern, recorded in the time domain, is converted into frequency-domain spectra via Fourier transform. Because of the finite maximum optical

https://doi.org/10.5194/egusphere-2025-5121
Preprint. Discussion started: 7 April 2026

path difference in the interferometer, the interferogram is truncated at both ends, causing a "sinc" function effect. Therefore, the instrument spectral response function has a "sinc" function shape.

In the fast radiative transfer model, channel transmittance is calculated by convolving the high-resolution monochromatic transmittance with the instrumental spectral response function of HIRAS. During the transformation of transmittance from monochromatic light (0.001 cm^{-1}) to the instrument spectral resolution (0.625 cm^{-1}), direct convolution with the sinc function derived from Fourier theory produces unphysical negative values in the results. To mitigate this issue, particularly the spectral leakage caused by sinc function sidelobes, we apply a Hamming window function (Harris, 1987) tailored to the instrument's specific characteristics. Hence, the instrumental line shape results from applying a cosine Fourier transform to the truncated interferogram. This study uses Eq. (11) to represent the instrumental spectral response function.

$$f_{Hm}(\nu) = \frac{a(\frac{27}{25}-\frac{16}{25}a^2\nu^2)\,\mathrm{sinc}(2\pi a\nu)}{1-4a^2\nu^2} \tag{11}$$

Where ν is the frequency, and a is the maximum optical path difference associated with the interferometric instrument detection.

The LBLRTM calculates the monochromatic atmospheric level-to-space transmittance for different gases at a spectral resolution of 0.001cm^{-1}. These high-resolution spectra are then convolved with the spectral response function defined in Eq. (12) to produce the channel-integrated transmittances in the HIRAS-II instrument:

$$R(\nu^*,\theta) = \int_{-\infty}^{+\infty} R(\nu,\theta) * f(\nu^*-\nu)d\nu \tag{12}$$

where f is the HIRAS-II spectral response function, ν^* is the channel center wavenumber, $R(\nu,\theta)$ is the level-to-space transmittance or radiance calculated by LBLRTM at 0.001cm^{-1} spectral resolution, and $R(\nu^*,\theta)$ is the transmittance or radiance of the instrument channel. The response function is identical for all channels, with the spectral response shown in Fig. 3.

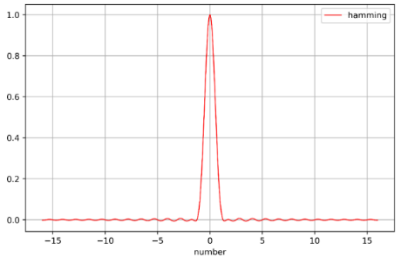

Figure 3: HIRAS Instrument Spectral Response Function (ISRF)

https://doi.org/10.5194/egusphere-2025-5121
Preprint. Discussion started: 7 April 2026

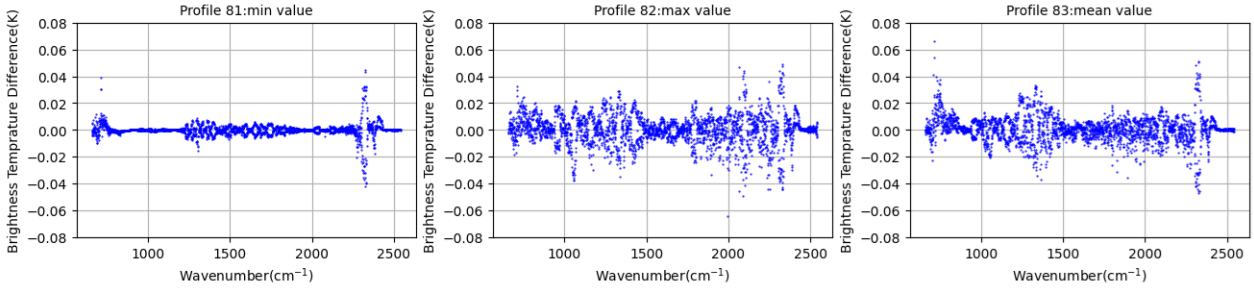

Figure 4: Impact of far-wing truncation on simulation accuracy

Among the 83 profile training datasets used for transmittance coefficients regression, three specific profiles (81, 82, and 83) represent the minimum, maximum, and mean values of atmospheric variables at each level, respectively. Fig. 4 compares the simulated brightness temperature differences among the three profiles under the far-wing truncation ranges relative to the centre wavenumbers of ±32 cm^{-1} and ±64 cm^{-1}, respectively. The results show that, regardless of the far-wing truncation range, the vast majority of channel brightness temperature differences are below 0.03 K, which is smaller than the instrument noise. Therefore, the ±32 cm^{-1} convolution range was selected for HIRAS data processing, as it provides comparable accuracy with lower computational cost.

3.3.2 Selection of HIRAS Clear-Sky Pixels

According to Wang et al. (2016), using co-located high-resolution imager cloud products (VIIRS) provides superior clear-sky detection for the CrIS sounder. Building on this finding, our study applies the same principle to develop a clear-sky detection scheme for HIRAS. For each HIRAS field of view (FOV), the algorithm identifies the co-located MERSI pixel, leveraging MERSI's superior spatial resolution. A sampling region centered on this MERSI pixel is then defined, with its spatial extent scaled to match the HIRAS FOV coverage based on their resolution ratio. Cloud mask data are extracted from a 43 × 43 pixel area within this region. The geometric overlap between the HIRAS FOV and the scaled MERSI sampling area is precisely calculated using the HIRAS field-of-view (FOV) parameters. A HIRAS FOV is classified as clear-sky only if all underlying MERSI cloud mask pixels within the overlapping zone are unanimously clear.

4 Validation of the Optimized Fast Transmittance Scheme Against LBLRTM Calculations

4.1 Impact of the Threshold Method (LSM1) on Simulation Accuracy

Based on 83 atmospheric profiles, profiles were selected using both unconstrained and threshold methods to calculate transmittance coefficients. The results were validated against LBLRTM benchmarks. At the left wing of the 6.7 μm absorption band, features due to SO_2, N_2, and CH_4 are present. These gases are all contained within a uniform mixture, which increases the complexity of transmittance calculations. The change in transmittance caused by the threshold method is shown in Fig. 5. Channel No. 1169 (central wavenumber 1380 cm^{-1}) lies on the far wing of the 6.7 μm absorption line, representing water vapor

https://doi.org/10.5194/egusphere-2025-5121
Preprint. Discussion started: 7 April 2026

absorption in the lower atmosphere, as shown in Fig. 5(a). Profile 82 represents the maximum values of all level variables among the set of 83 profile samples. At this point, applying the threshold has a negligible effect on fast transmittance calculations for this profile type. The impact of threshold magnitude is essentially the same as that seen for dry profiles, as shown by Profile 81. As the water vapor content decreases, the impact of the threshold on transmittance calculation accuracy increases, but it is mainly limited to altitudes below 600 hpa, which corresponds roughly to the channel detection height (peak height of the weighting function). Furthermore, the lower the water vapor content, the clearer the improvement in transmittance calculation accuracy. Profile 81 has the lowest variable values among sample profiles, and here the threshold's effect is strongest. Compared with the transmittance deviation calculated without constraints, the fast transmittance calculated using a threshold constraint closely matches that from LBLRTM. In Fig. 5(b), channel 1239 (central wavenumber 1423.75 cm^{-1}) represents water vapor absorption in the mid-level atmosphere. For profiles with above-average water vapor content (water-rich profiles), forward model accuracy matches that in Fig. 5(a). For water-poor profiles below the average, the threshold effect becomes stronger. As water vapor content decreases along the profile, the altitude where threshold-induced transmittance deviation increases gradually rises. At the 81st profile, the highest altitude where the threshold method improves transmittance deviation does not exceed the channel detection height. In Fig. 5(c), Channel 1372 (central wavenumber 1506.875 cm^{-1}) lies within the 6.7 μm absorption line used to detect upper-level water vapor. The effect of the threshold on forward modeling accuracy is similar to Fig. 5(a) and (b), but its influence is more pronounced.

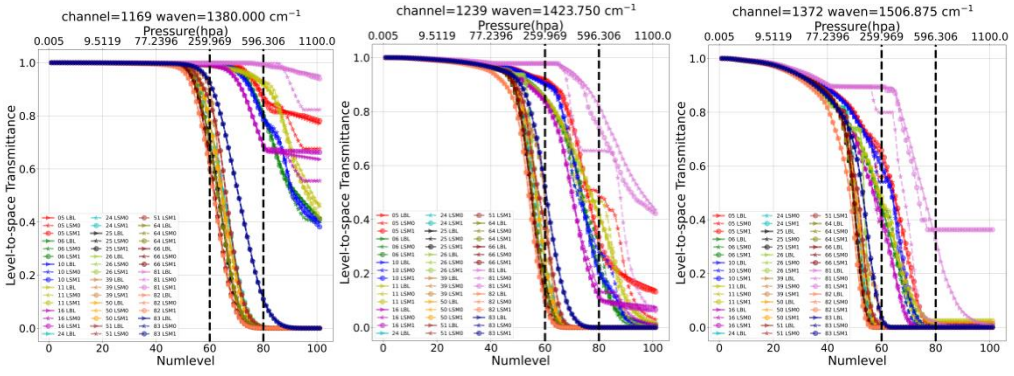

Figure 5: Comparison of fast transmittance calculated by different schemes for LSM0 (pentagram) and LSM1 (circle) versus LBLRTM (triangle) transmittance across three channels (1380 cm^{-1}(a), 1423.75 cm^{-1}(b), 1506.875 cm^{-1}(c)).

Fig. 6 presents a comparative analysis of transmittance versus atmospheric pressure for the channel at the right end of the 6.7-μm absorption line. Within this spectral range, only the weak absorption lines of NO_2 and CH_4 lie in the near-wing region of the 6.7 μm absorption line. The transmittance calculated by the threshold method and by LBLRTM show nearly identical distributions across atmospheric pressure, consistent with Fig. 5. This suggests that trace gases in either the far-wing or near-wing regions do not affect the accuracy improvement achieved by the threshold method.

https://doi.org/10.5194/egusphere-2025-5121
Preprint. Discussion started: 7 April 2026

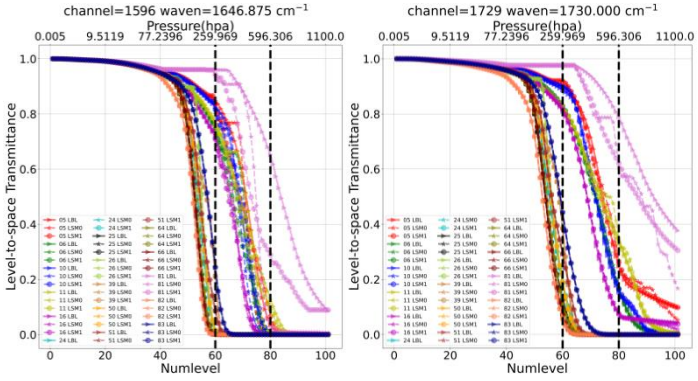

Figure 6: Comparison of fast transmittance calculated by different methods (LSM0 indicated by pentagrams, LSM1 by circles) versus LBLRTM (triangles) for the 1646.875cm⁻¹ and 1730cm⁻¹ channels, showing transmittance variation with pressure.

For 83 atmospheric profiles, level-to-space atmospheric transmittance was calculated at six satellite zenith angles, producing a total of 498 atmospheric samples. At each isobaric surface, this resulted in a system of 498 second-order linear equations. Analysis indicates that when the cumulative transmittance from a level to the top of the atmosphere is less than 10^{-4}, the cumulative transmittance from the level below to the top of the atmosphere may become negative. In consideration of both instrument characteristics and transmittance variation patterns, this study adopts a semi-empirical threshold of 10^{-4} as the screening criterion to filter out physically meaningless transmittance. The Fig. 7 shows that for each profile, there is an identified position indicating the pressure height above which the profile participates in the training of the corresponding channel, and below which the profile does not participate in the training of the corresponding channel: blue for channel 1169, brown for channel 1239, green for channel 1372, yellow for channel 1596, and red for channel 1729. On the vertical axis, 0 indicates the top of the atmosphere, and 100 indicates the surface. As pressure height increases, the number of samples used decreases gradually. Applying the threshold method to filter samples reveals a strong correlation between the number of profiles used in calculations and the absorption characteristics of the channels in these levels: The stronger the absorption, the fewer profiles are included in the training for the middle and lower tropospheric layers. All upper-atmosphere profiles can be retained; however, in the lower atmosphere, retainable samples may drop to fewer than ten. The number of retained samples is higher for channels in absorption line wing regions than for those in peak regions. Moreover, retained sample altitudes are lower for wing-region channels (up to 800 hPa) than peak-region channels (up to 600 hPa). This occurs because, as a channel approaches an absorption line peak region, more samples below its detection altitude have near-zero transmittance and are thus filtered out by thresholding. Additionally, sample retention varies between the left and right ends of peak regions. This can be explained as follows: as the channel moves toward the absorption line peak region, the number of samples with near-zero transmittance below the channel detection altitude gradually increases, which results in more samples being affected by threshold filtering. Additionally, the number of retained samples varies between the left and right ends of the peak region.

https://doi.org/10.5194/egusphere-2025-5121
Preprint. Discussion started: 7 April 2026

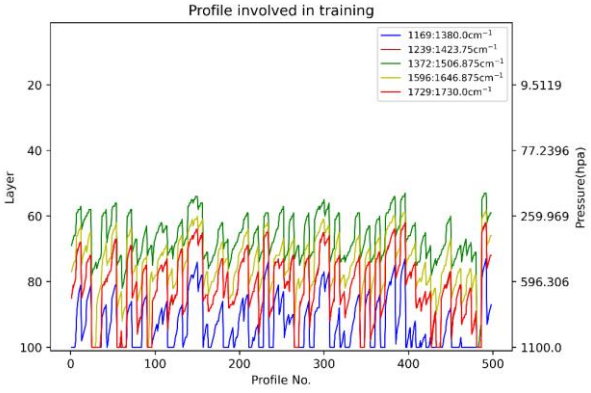

Figure 7: Profile positions of different channels and atmospheric layers participating in statistics under a threshold condition of 10^{-4}.

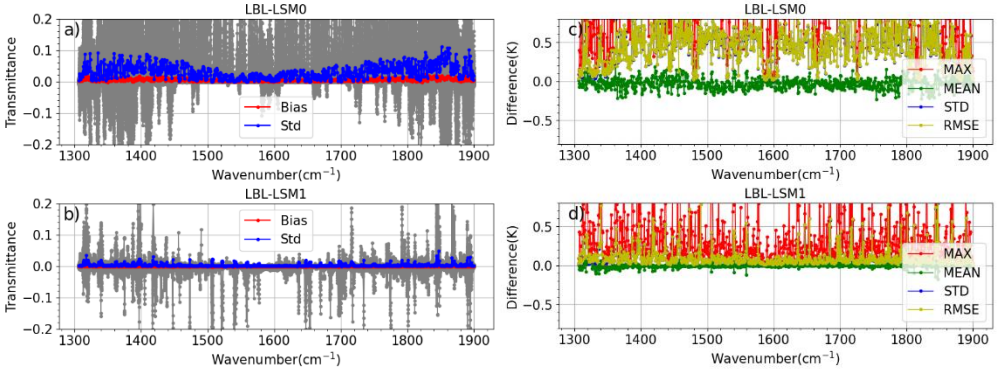

Figure 8: Variation of the difference between fast transmittance calculated by LSM0 and LSM1 schemes and transmittance calculated by LBLRTM, along with the difference in brightness temperature, across channels.

In Fig. 8, the surface emissivity for all channels is uniformly set to 0.98 to eliminate its influence on forward modeling results across different schemes. The deviations between the 6.7 μm absorption line spectrum transmittances at the top of the atmosphere calculated by LSM0 and LSM1 for all channels and the LBLRTM results are shown in Fig. 8(a) and (b). In the figure, gray indicates the transmission deviation of all profiles calculated by LSM0 and LSM1 relative to LBLRTM. LSM0 forward simulation exhibits positive deviations in the absorption line peak and near-wing regions, while negative deviations occur in the distant wing regions. The deviation distribution of LSM1 is more uniform, though negative deviations increase in the peak region. The standard deviation of LSM1 is significantly reduced from approximately 0.1K for LSM0 to less than 0.05K, with a uniform distribution across spectral channels. Unlike LSM0, the standard deviation in the absorption line wings does not exceed that in the peak regions. The deviation distribution shows similar characteristics to the standard deviation. Fig. 8(c) and (d) show the deviation distributions of brightness temperature in the mid-wave channels for LSM0 and LSM1 forward modeling, respectively. As shown in Fig. 8, for both LSM0 and LSM1 calculations of brightness temperature, the maximum deviation from LBLRTM simulated brightness temperature exceeds 0.5K across all 83 profiles. Regarding average deviation, LSM1 shows an average value around -0.1K, which is significantly smaller than the -0.2K deviation of

https://doi.org/10.5194/egusphere-2025-5121
Preprint. Discussion started: 7 April 2026

LSM0. At the left end of the 1350 cm^{-1} range, the deviations between the two methods are comparable. Similarly, at the left end of the 1350 cm^{-1} region, the deviations between the two schemes are not markedly different. In terms of standard deviation and root mean square error distributions, LSM1 also significantly outperforms LSM0. These results collectively demonstrate that the threshold method effectively improves forward model accuracy.

4.2 Impact of the Threshold and Weight Coefficient Method 1 (LSM2) On Simulation Accuracy

In the LSM2 experiments, a weight constraint was additionally applied to the threshold method-constrained training profiles, as shown by the right-hand side term in Eq. (6). In Fig. 9, the difference between LSM1 and LSM2 is negligible in the far-wing region to the left of the 6.7 μm absorption line, and their correction effects on transmittance are identical to those shown in Fig. 5(a). For the extremely dry atmospheric conditions represented by profile 81, LSM2 shows greater discrepancies from LBL transmittance at lower atmospheric levels and near the channel detection altitude. At 1506.875 cm^{-1}, LSM2 exhibits negative deviations relative to LBL results across all altitudes from 300 hPa to 600 hPa, clearly contrasting with LSM1 positive deviations. Moreover, below 700 hPa, LSM1 maintains a constant transmittance of 0.38, differing significantly from LBL transmittance, which monotonically approaches zero. At this point, LSM2 results better match the actual atmospheric transmission distribution, indicating that LSM2 significantly improves the forward modeling accuracy of transmittance in the lower atmosphere for the 6.7 μm absorption line peak region channel under extremely dry conditions.

Fig. 10 shows the transmittance distribution for the right-end channel of the 6.7 μm absorption line. For extremely dry atmospheres, the deviation between LSM2 and LBL remains smaller than that of LSM1 below 250 hPa. Between 300 hPa and 600 hPa, the deviation between LSM2 transmittance and LBL gradually decreases. Below 600 hPa, it essentially overlaps with the LBL transmittance profile, with the largest discrepancy occurring in the low-vapor-content atmosphere of profile 81. The maximum deviation between LSM0/LSM1 and LBL transmittance calculations occurs below 900 hPa, increasing at lower altitudes. However, the difference between LSM2 and LBL remains largely constant with height and is smaller than that of LSM1.

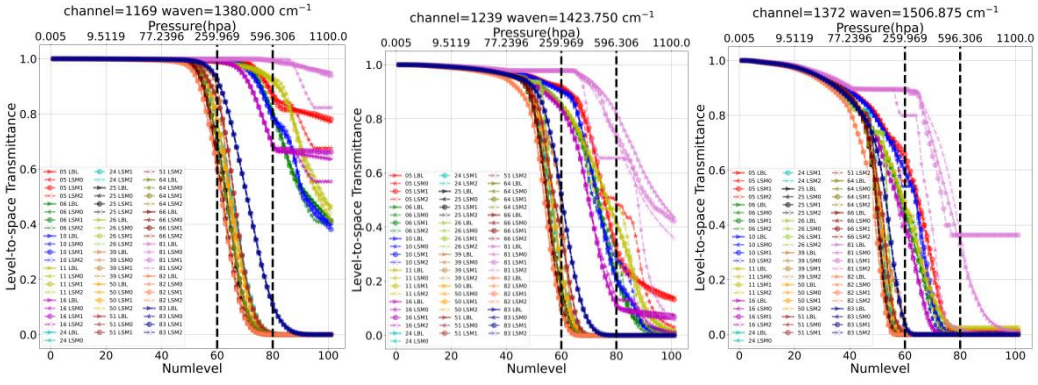

Figure 9: Comparison of fast transmittance calculated by LSM0 (★), LSM1 (○), LSM2 (×), and LBLRTM (△) across three channels (1380 cm^{-1}, 1423.75 cm^{-1}, 1506.875 cm^{-1}) versus pressure.

https://doi.org/10.5194/egusphere-2025-5121
Preprint. Discussion started: 7 April 2026

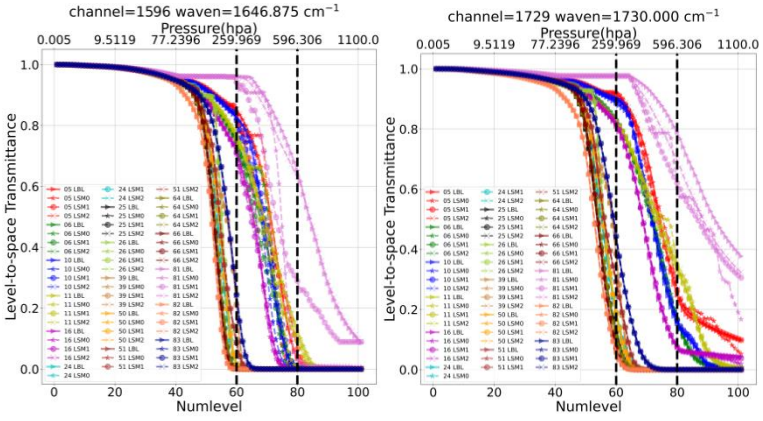

Figure 10: Comparison of fast transmittance calculated by LSM0 (★), LSM1 (○), LSM2 (×), and LBLRTM (△) across three channels (1646.875 cm⁻¹ 、 1730 cm⁻¹) versus pressure.

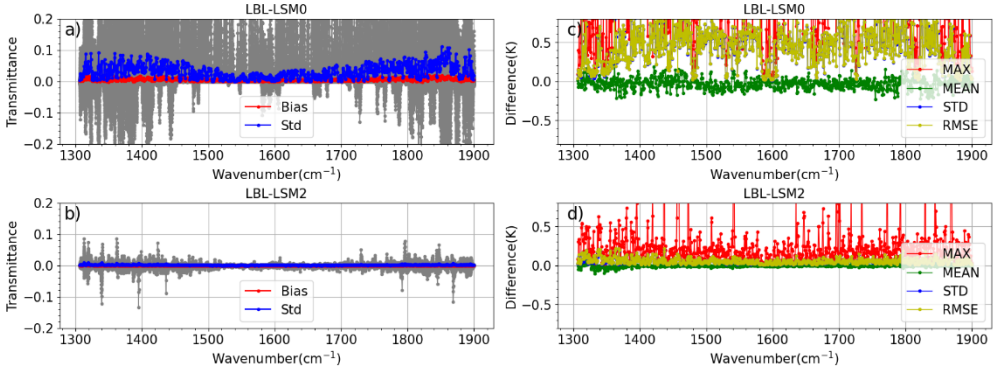

Figure 11: Differences in fast transmittance (LSM0/LSM2 vs. LBLRTM) and brightness temperature across all channels.

The configuration in Fig. 11 is essentially identical to that of Fig. 8, showing the distribution of channel transmittance and simulated brightness temperature deviations for LSM0, LSM2, and LBL across channels at the top of the atmosphere. The transmittance deviation between LSM0 and LBL exceeds 0.2 in most channels, while the brightness temperature bias and standard deviation remain within 1 K. After thresholding combined with weighting coefficient correction, the maximum channel transmittance deviation falls below 0.1, as shown in Fig. 11(b). The mean and standard deviation of transmittance in mid-wave spectral channels are less than 0.02. As shown in Fig. 11(d), the mean and standard deviation of brightness temperature differences are both below 0.2 K. In Fig. 11(b), the transmittance deviation distribution of LSM2 at the left end of 1380 cm⁻¹ is identical to that of LSM1, indicating that weight correction does not significantly improve forward modeling accuracy for overlapping absorption spectra of trace gases and water vapor. In other mid-wave spectral channels, LSM2 shows a marked improvement in forward modeling accuracy compared to LSM0. Furthermore, compared to the forward modeling accuracy of LSM1 in Fig. 8(b) and (d), LSM2 exhibits a more uniform deviation distribution across the mid-wave spectrum, eliminating the large deviations observed in some spectral channels of LSM1.

https://doi.org/10.5194/egusphere-2025-5121
Preprint. Discussion started: 7 April 2026

4.3 Impact of the Threshold And Weight Coefficient Method 2 (LSM3) On Simulation Accuracy

Fig. 12 shows the effect of LSM3 on the transmittance profile of the left-end channel of the 6.7μm absorption peak compared to LSM2, LSM1, and LSM0, using the same settings as in Fig. 5. As shown in Fig. 12, the improvement in transmittance by LSM3 remains concentrated in the low-to-mid troposphere with low water vapor content, and the altitude of influence closely correlates with the channel detection altitude. The improvements of LSM3 compared to LSM0 and LSM1 are significant. The transmittance profile calculated by LSM3 almost coincides with that of LSM2. Fig. 13 compares transmittance for the right-end channel of the 6.7 μm absorption peak, using the same settings as in Fig. 6.

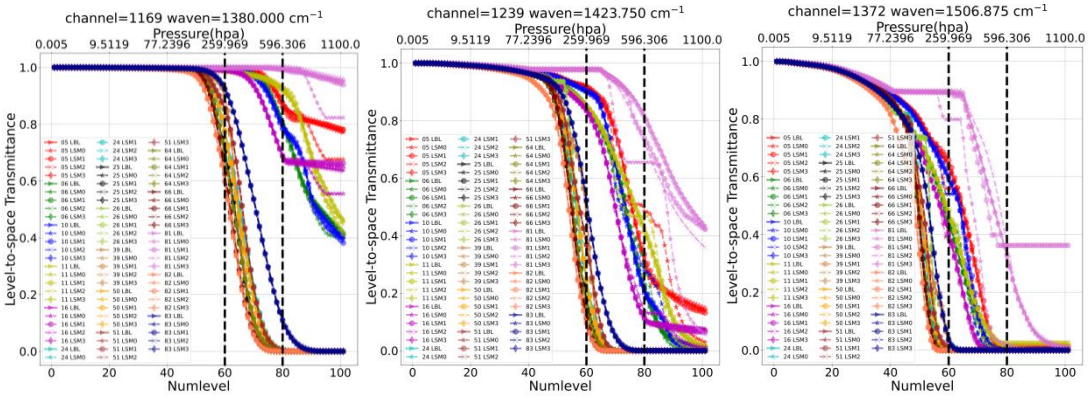

Figure 12: Comparison of fast transmittance calculated by LSM0 (★), LSM1 (○), LSM2 (×), LSM3(◇) and LBLRTM (△) across three channels (1380 cm⁻¹, 1423.75 cm⁻¹, 1506.875 cm⁻¹) versus pressure.

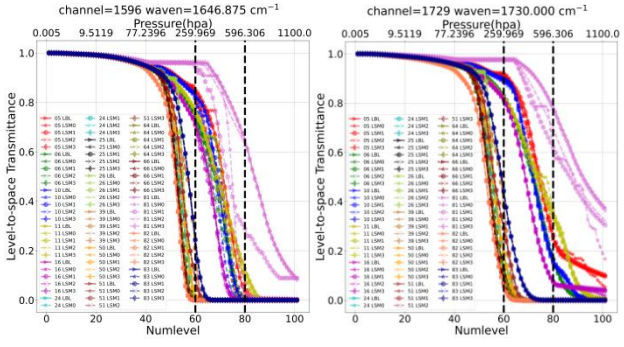

Figure 13: Comparison of fast transmittance calculated by LSM0 (★), LSM1 (○), LSM2 (×), LSM3(◇) and LBLRTM (△) across two channels (1646.875 cm⁻¹, 1730 cm⁻¹) versus pressure.

https://doi.org/10.5194/egusphere-2025-5121
Preprint. Discussion started: 7 April 2026

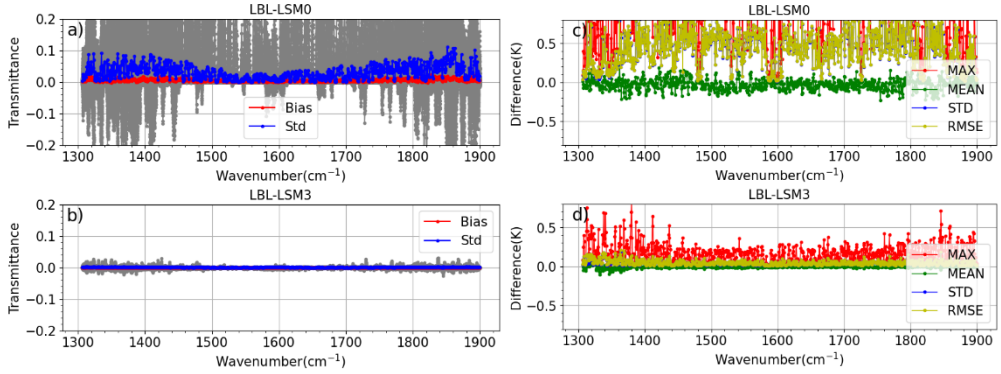

Figure 14: Differences in fast transmittance (LSM0/LSM3 vs. LBLRTM) and brightness temperature across all channels.

Fig. 14 shows the statistical deviation of total channel transmittance and brightness temperature for different LSM0 and LSM3 schemes, using the same settings as in Fig. 8. As shown, compared to the transmittance deviation in LSM2 from Fig. 11, the deviation in LSM3 is further reduced. In the brightness temperature deviation statistics in Fig. 8(d), the mean RMSE for the mid-wave spectrum (1300~1900 cm^{-1}) of LSM1, LSM2, and LSM3 progressively decreases from 0.1 K to 0.05 K and 0.045 K, respectively, while the mean maximum value decreases from 0.45 K to 0.22 K and 0.15 K. This indicates that combining the threshold method with weighting coefficients for least-squares solutions can further reduce forward modeling deviations in HIRAS-II mid-wave channels, with the LSM3 scheme producing the smallest error distribution.

5 Evaluation of the Optimized Scheme Using FY-3F HIRAS-II Satellite Observations

Fig. 15 shows selected channels from HIRAS-II in the far-wing region and at the absorption peak of the 6.7μm absorption line. Using FY-3F HIRAS-II ascending orbit clear-sky observation data from August 1, 2024, and February 1, 2025, the distribution characteristics of observational simulation deviations for LSM3, RTTOV, and HIRAS-II during summer and winter are analyzed. Among these, the 1380 cm^{-1} and 1730 cm^{-1} channels are lower-level detection channels located at the far wing of the 6.7 μm absorption line. The 1423.75 cm^{-1} and 1646.875 cm^{-1} channels are mid-level detection channels, while 1506.875 cm^{-1} is an upper-level detection channel positioned near the absorption line peak. In Fig. 15(a), the left column shows the deviation distributions for August 1 (summer), while the right column shows those for February 1 (winter). The first row depicts deviations between observations and RTTOV simulated brightness temperatures; the second row shows deviations between observations and LSM3 results; and the third row illustrates deviations between RTTOV simulated brightness temperatures and LSM3 outputs. The figures show that, for both ocean and land surfaces and in both winter and summer, the deviation distribution trends for LSM3 simulated brightness temperatures are essentially identical to those of RTTOV. The root-mean-square error (RMSE) for both simulated brightness temperatures is about 1 K, with the summer RMSE larger than the winter RMSE. The third row shows that the deviation between LSM3 and RTTOV is near zero, indicating that the LSM3 simulated deviation closely matches that of RTTOV. Fig. 15(c) presents the deviation distribution for the 1646.875 cm^{-1}

https://doi.org/10.5194/egusphere-2025-5121
Preprint. Discussion started: 7 April 2026

channel, using the same settings as (a). The deviation characteristics of LSM3 versus observations and RTTOV versus observations are similar, and both show larger mean and RMSE than the 1380 cm^{-1} channel. Fig. 15(b) shows the 1506.875 cm^{-1} channel with the same settings as Fig. 15(a). The deviation distributions for LSM3 versus observations and RTTOV versus observations resemble those in Fig. 15(a) and (c). However, when comparing LSM3 with RTTOV simulated brightness temperatures, RTTOV has a larger mean and RMSE than LSM3 in both winter and summer by about 0.1 K. The deviation distributions for the 1423.75 cm^{-1} and 1730 cm^{-1} channels, located at the right side of the 6.7 μm absorption peak, are the same as those for the 1380 cm^{-1} and 1646.875 cm^{-1} channels. Therefore, analysis is omitted here (figure omitted).

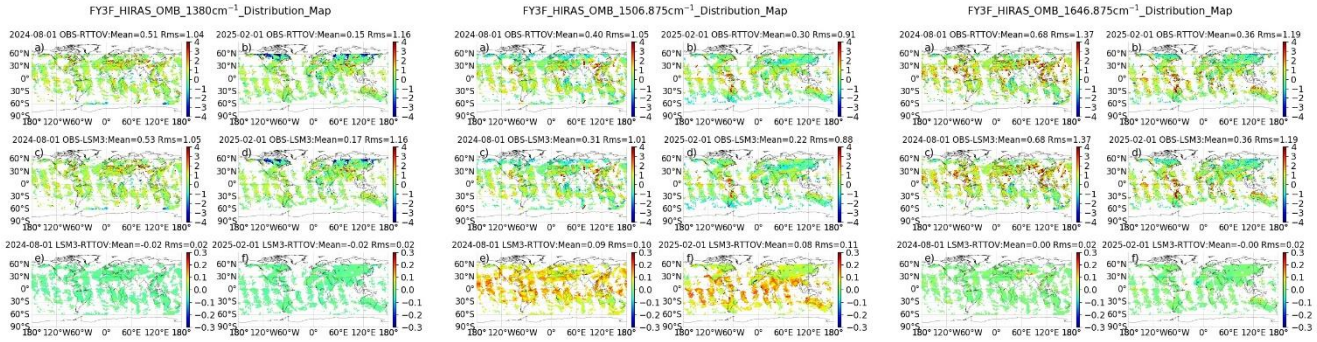

Figure 15: Global distribution of brightness temperature differences between FY-3F HIRAS-II simulated clear-sky data and mid-to-low latitude observations, based on ERA-5 reanalysis data, for the 1380 cm^{-1} (a), 1506.875 cm^{-1} (b), and 1646.875 cm^{-1} (c) channels.

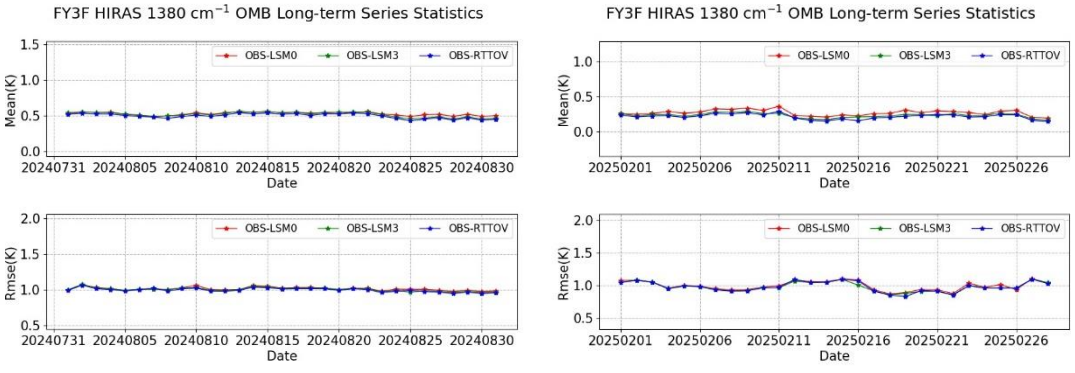

https://doi.org/10.5194/egusphere-2025-5121
Preprint. Discussion started: 7 April 2026

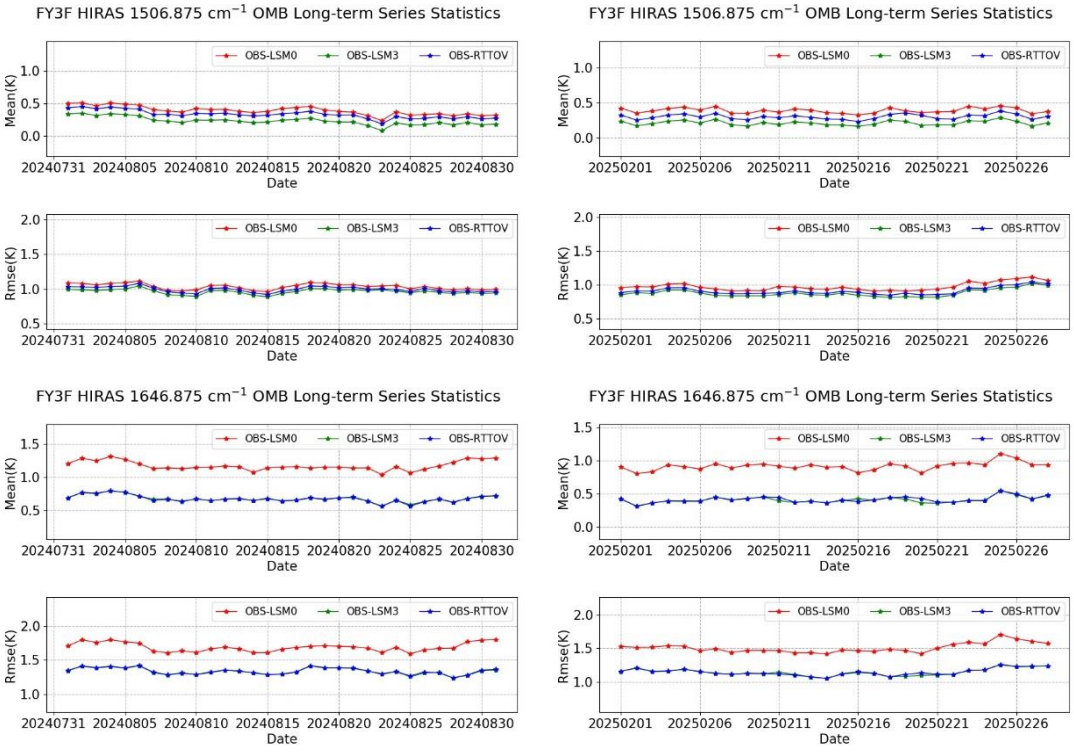

Figure 16: Long-term bias and RMSE of OMB over time for the LSM0, LSM3, and RTTOV models. (1380 cm^{-1}(a), 1506.875 cm^{-1}(b), 1646.875 cm^{-1}(c)).

Representative summer observation months were obtained from FY-3F HIRAS-II data in August 2024, while winter months came from observations in February 2025. The daily distribution of deviations between observed and simulated brightness temperatures from the LSM0, LSM3, and RTTOV models is shown in Fig. 16. The channel at 1380 cm^{-1} used for long-term time series analysis of observation minus background (OMB) in Fig. 16(a) is the same as in Fig. 15(a). The left column shows summer deviation distributions, while the right column shows winter distributions. The first row shows the long-term mean OMB over time, and the second row shows OMB RMSE variations over time. As shown in Fig. 16, simulation errors for all three forward modeling methods are smaller in winter than in summer. The mean and root mean square errors of the OMB for both LSM3 and RTTOV are essentially the same. Regardless of using LSM3 or RTTOV, their forward-modeling mean error and RMSE are smaller than those of LSM0. Fig. 16(b) shows results for the strong water vapor absorption line at 1506.875 cm^{-1} with settings identical to Fig. 16(a). The figure shows that RMSE time evolution curves for LSM3 and RTTOV OMB nearly overlap, but the mean OMB for LSM3 is slightly lower by about 0.1K, suggesting that LSM3 has a smaller forward-modeling bias than RTTOV near the 6.7 μm absorption peak channel. Fig. 16(c) presents data for the 1646.875 cm^{-1} channel. RMSE over time for LSM3 and RTTOV OMB remains nearly identical, while both mean OMB and RMSE for LSM0 are significantly larger than those of LSM3 and RTTOV. Deviation distributions at 1423.75 cm^{-1} and 1730 cm^{-1} in the wing region of the 6.7 μm absorption peak are consistent with those observed at 1646.875 cm^{-1} and 1380 cm^{-1}, so they are omitted here.

https://doi.org/10.5194/egusphere-2025-5121
Preprint. Discussion started: 7 April 2026

6 Synthesis and Discussion of Forward Model Improvements

In the transmittance calculation for infrared atmospheric remote sensing, the presence of negative values in spectral response function will trigger a series of chain problems, making their proper handling essential. The spectral response function of hyperspectral infrared sounders (such as HIRAS-II) contains negative values due to the limitations of instrument design and spectral calibration processes. During the convolution process that converts theoretical monochromatic transmittance into instrument-measured transmittance, these negative response values can lead to non- physical negative transmittance, particularly in strong absorption channels.

For example, 1506.875 cm^{-1} is the strong absorption channel for water vapor. Under conditions of abundant water vapor content, transmittance in this band becomes extremely small in the middle and lower atmosphere. The presence of negative values not only violates the basic physical Beer–Lambert law, which requires transmittance should range between 0 and 1, but also severely distorts the true absorption characteristics of water vapor. Moreover, the handling of small transmittance values in strong absorption channels adds another difficulty. The extremely small transmittance magnitudes (close to 0) in these channels are inherently prone to numerical instability. When combined with the negative value issues, this instability is significantly amplified, resulting in larger deviations in transmittance calculations. The coexistence of unphysical negative values and the difficulty of handling extremely small quantities significantly increases the challenge of achieving accurate radiative transfer simulations.

When a threshold of 10^{-4} is applied, the accuracy of fast transmittance coefficient calculations improves significantly for certain layers. However, beyond approximately 70 layers, the layer-by-layer error accumulates, leading to increasing deviations in level-to-space transmittance. Although the threshold partially alleviates the negative value problem, it introduces new challenges. The threshold value represents a cutoff pressure level height for water vapor absorption channels. A larger threshold corresponds to a lower pressure at the cutoff level. If no training samples exist below this cutoff, the model implicitly sets the transmittance of all lower layers to 1, causing the level-to-space transmittance to remain constant below that point. As a result, for strong absorption channels, the accuracy in the middle and lower troposphere of dry profiles is significantly degraded. In contrast, for weak absorption channels, the transmittance decreases more slowly, and the cumulative transmittance near the surface remains relatively large, making the threshold's impact much smaller.

Therefore, LSM1 adopts a semi-empirical threshold of 10^{-4} for filtering the statistical regression samples. However, because the lower atmospheric layers contribute relatively little to the total absorption, it is unnecessary to rely solely on rigid threshold-based exclusion. Instead, lowering the threshold and introducing a weighting scheme can reduce the influence of the lowest layers without depending exclusively on the threshold, as implemented in LSM2 and LSM3.

This study optimizes the transmittance coefficient solution for the 6.7 μm absorption channel of HIRAS-II using two approaches: (1) threshold-based sub-selection of training samples, and (2) weighting in the least-squares solution. Comparisons with line-by-line (LBL) calculations and HIRAS-II observations lead to the following conclusions:

First, introducing threshold-based sample selection significantly improves the accuracy of LSM1 in the upper and middle

https://doi.org/10.5194/egusphere-2025-5121
Preprint. Discussion started: 7 April 2026

atmosphere for the 6.7 μm channel, covering both the absorption peak and wing regions. This improvement is robust across both water-poor and water-rich atmospheric conditions. The threshold effectively removes abnormal profiles that tend to produce unphysical negative values, ensuring that the training dataset better matches the actual atmospheric characteristics observed by HIRAS-II. Quantitative comparisons with LBL show that the RMSE of LSM1 is reduced relative to the unfiltered model (LSM0), confirming the effectiveness of the sample selection strategy.

Second, incorporating weighting corrections into the least-squares solutions further produce a step-wise improvement beyond LSM1. Compared with the unweighted models (LSM0 and LSM1), the weighted models (LSM2 and LSM3) achieve higher simulation accuracy in both transmittance and brightness temperature calculations. LSM3 outperforms LSM2. The proposed weighting scheme is physically meaningful: In strong absorption regions where transmittance is very small, it increases the weight of samples with larger transmittance, suppressing numerical fluctuations; in weaker absorption regions (line wings), it maintains balanced weights to preserve adaptability. As a result, LSM3 shows reduced bias and RMSE in brightness temperature at the absorption peak, demonstrating that weighting effectively compensates for the limitations of unweighted least squares methods in handling small transmittance values.

Third, validation against actual HIRAS-II observations confirms the practical application value of LSM3. In the wing region of the 6.7 μm channel, LSM3's deviations (both brightness temperature and transmittance) closely match those of RTTOV, with brightness temperature differences below 0.1 K and transmittance differences near zero. More importantly, in the absorption peak region, LSM3 significantly outperforms RTTOV, demonstrating its ability to simultaneously address negative-value interference and small-value instability. Long-term validation further shows that LSM3 maintains stable performance across different times and locations.

In summary, introducing thresholds and weighting strategies substantially improves the accuracy of transmittance coefficient calculations for the 6.7 μm HIRAS-II channel. The proposed scheme clarifies the mechanisms by which sample selection and weighting influence accuracy and provides a reference for addressing negative-value and small-value issues in other instruments and spectral bands. From an application perspective, the optimized model (LSM3) facilitates enhanced data assimilation for FY-3 HIRAS. Beyond the HIRAS-II on FY-3F, this optimization method is also directly applicable to fast transmittance calculations for other trace gas absorption bands (e.g., CO_2, O_3) and to other platforms such as FY-3D and FY-3E, providing robust support for future atmospheric constituent retrieval applications.

code and data availability

The source code for the rapid transmittance algorithm, along with the processed atmospheric profile datasets used for testing and validation in this study, is publicly available on Zenodo: Zhang, P.X. (2025). Optimization of the Fast Layer Transmittance Algorithm in RTTOV for Strong Water Vapor Absorption Channels of the FY-3 HIRAS-II Instrument Using LBLRTM v12.11. Zenodo. https://doi.org/10.5281/zenodo.18263685.

https://doi.org/10.5194/egusphere-2025-5121
Preprint. Discussion started: 7 April 2026

Author contributions

PXZ conducted the methodological research, performed the experiments, developed the model code and implemented the simulations, and drafted the initial manuscript. PZ conceived and defined the overall research goals, designed the experiments, and revised and polished the manuscript. GM co-designed the experiments, supervised and guided the experimental implementation, verified the rationality of the simulation results, and revised and polished the manuscript. RL reviewed the manuscript and provided critical comments and experimental suggestions. LL assisted PXZ in understanding the instrument principles and designing the spectral response functions. WB assisted PXZ in verifying the rationality of the line-by-line integration simulation results. CQ assisted PXZ in learning the construction of the HIRAS clear-sky detection methods.Competing interests

The authors declare that they have no conflict of interest.

Acknowledgements

We acknowledge Atmospheric and Environmental Research, Inc. (AER) for providing LBLRTM v12.11 (license: https://github.com/AER-RC/LBLRTM/blob/master/LICENSE.md), which served as the reference for transmittance validation in this study. We also extend our thanks to the NWP SAF and the RTTOV development team for making the RTTOV model available (https://www.nwpsaf.eu/site/software/rttov/), which was instrumental in validating the fast transmittance algorithm presented here.

Financial support

This work was supported by the National Natural Science Foundation of China (grant nos. U2442214 and 42475170).

References

Alvarado, M., Payne, V., Mlawer, E., Uymin, G., Shephard, M., Cady-Pereira, K., Delamere, J., and Moncet, J.-L.: Performance of the Line-By-Line Radiative Transfer Model (LBLRTM) for temperature, water vapor, and trace gas retrievals: recent updates evaluated with IASI case studies, Atmospheric Chemistry and Physics, 13(13), 6687-6711, https://doi.org/10.5194/acp-13-6687-2013, 2013.

Bai, W., Zhang, P., Zhang, W., Ma, G., and Qi, C.: A model for accurately calculating hyper-spectral, middle-shortwave infrared radiative transfer for remote sensing, Science China Earth Sciences, 61, 317-326, https://doi.org/10.1007/s11430-017-9100-6, 2017.

Bai, W., Zhang, P., Zhang, W., Li, J., Ma, G., Qi, C., and Liu, H.: Jacobian matrix for near-infrared remote sensing based on vector radiative transfer model, Science China Earth Sciences, 63, 1353-1365, https://doi.org/10.1007/s11430-019-9586-7, 2020.

Bormann, N., Salmond, D., Matricardi, M., Geer, A., and Hamrud, M.: The RTTOV-9 upgrade for clear-sky radiance assimilation in the IFS, ECMWF Technical Memorandum, 586, https://doi.org/10.21957/gqpyuvskj, 2009.

Clough, S. A., Shephard, M. W., Mlawer, E. J., Delamere, J. S., Iacono, M. J., Cady-Pereira, K., ... & Brown, P. D. Atmospheric radiative transfer modeling: A summary of the AER codes. Journal of Quantitative Spectroscopy and Radiative Transfer, 91(2), 233-244, 2005.

https://doi.org/10.5194/egusphere-2025-5121
Preprint. Discussion started: 7 April 2026

Chevallier, F., Di Michele, S., and McNally, A. P.: Diverse profile datasets from the ECMWF 91-level short-range forecasts, NWP SAF Technical Report, 10, https://www.ecmwf.int/en/elibrary/73985-diverse-profile-datasets-ecmwf-91-level-short-range-forecasts, 2006.

Di, D., Li, J., Han, W., Bai, W., Wu, C., and Menzel, W. P.: Enhancing the Fast Radiative Transfer Model for FengYun-4 GIIRS by Using Local Training Profiles, Journal of Geophysical Research: Atmospheres, 123, https://doi.org/10.1029/2018jd029089, 2018.

Dhudia, A.: The Reference Forward Model (RFM). Journal of Quantitative Spectroscopy & Radiative Transfer, 186:243-253, https://doi.org/10.1016/j.jqsrt.2016.06.018, 2017.

Eyre, J. R. and Woolf, H. M.: Transmittance of atmospheric gases in the microwave region: a fast model, Appl. Opt., 27, 3244-3249, https://doi.org/10.1364/AO.27.003244, 1988.

Eyre J. R. A fast radiative transfer model for satellite sounding systems. ECMWF, Research Dept., Tech. Memo., 176, 1991.

Eyre, J. R., Kelly, G. A., McNally, A. P., Andersson, E., and Persson, A.: Assimilation of TOVS radiance information through one-dimensional variational analysis, Quarterly Journal of the Royal Meteorological Society, 119, 1427-1463, https://doi.org/10.1002/qj.49711951411, 1993.

Eyre, J. R., English, S. J., and Forsythe, M.: Assimilation of satellite data in numerical weather prediction. Part I: The early years, Quarterly Journal of the Royal Meteorological Society, 146, 49-68, https://doi.org/10.1002/qj.3654, 2020.

Eyre, J.R., Bell, W., Cotton, J., English, S., Forsythe, M., Healy, S., and Pavelin, E.: Assimilation of satellite data in numerical weather prediction. Part II: Recent years, Quarterly Journal of the Royal Meteorological Society, 148, https://doi.org/10.1002/qj.4228, 521-556, 2021.

Hannon, S. E., Strow, L. L., and McMillan, W. W.: Atmospheric infrared fast transmittance models: A comparison of two approaches, Optical Spectroscopic Techniques and Instrumentation for Atmospheric and Space Research II, SPIE, 2830, 94-105, https://doi.org/10.1117/12.256106, 1996.

Harris, F. J.: Multirate FIR filters for interpolating and desampling, in: Handbook of Digital Signal Processing, Academic Press, 173–287, https://doi.org/10.1016/B978-0-08-050780-4.50008-4, 1987.

Hocking, J., Vidot, J., Brunel, P., Roquet, P., Silveira, B., Turner, E., and Lupu, C.: A new gas absorption optical depth parameterisation for RTTOV version 13, Geoscientific Model Development, 14, 2899-2915, https://doi.org/10.5194/gmd-14-2899-2021, 2021.

Hocking, J., Candy, B., Dell, M., Rundle, D., Geer, A., Lupu, C., Scanlon, T., Turner, E., Borderies, M., Chambon, P., Lalande, J.-M., Vidot, J., Baur, F., Köpken-Watts, C., Raisig, P., Scheck, L., Stiller, O., Stumpf, C., Barlakas, V., Borbas, E., Labonnote, L., and Mangla, R..: RTTOV v14 Science and Validation Report (Version 1.0.1), available at: https://nwp-saf.eumetsat.int/site/download/documentation/rtm/docs_rttov14/rttov14_svr.pdf (last access: 10 January 2026), 2025.

Johnson, B. T., Dang, C., Stegmann, P., Liu, Q., Moradi, I., and Auligne, T.: The Community Radiative Transfer Model (CRTM): Community-focused collaborative model development accelerating research to operations. Bulletin of the American Meteorological Society, 104(10), E1817-E1830, https://doi.org/10.1175/BAMS-D-22-0015.1, 2023.

Kleespies, T. J., van Delst, P., McMillin, L. M., and Derber, J.: Atmospheric transmittance of an absorbing gas. 6. OPTRAN status report and introduction to the NESDIS/NCEP community radiative transfer model, Appl Opt, 43, 3103-3109, https://doi.org/10.1364/ao.43.003103, 2004.

Li, J., Li, Z., Wang, P., Schmit, T. J., Bai, W., and Atlas, R.: An efficient radiative transfer model for hyperspectral IR radiance simulation and applications under cloudy-sky conditions, Journal of Geophysical Research: Atmospheres, 122, 7600-7613, https://doi.org/10.1002/2016JD026273, 2017.

Li, S., Hu, H., Fang, C., Wa*ng, S.*, Xun, S., He, B., Wu, W., and Huo, Y. Hyperspectral Infrared Atmospheric Sounder (HIRAS) Atmospheric Sounding System. Remote Sensing, 14(16), 3882, https://doi.org/10.3390/rs14163882, 2022.

Matricardi, M. and Saunders, R.: Fast radiative transfer model for simulation of infrared atmospheric sounding interferometer radiances, Appl. Opt., 38, 5679-5691, https://doi.org/10.1364/AO.38.005679, 1999.

Matricardi, M.: RTIASI-4, a new version of the ECMWF fast radiative transfer model for the infrared atmospheric sounding interferometer, European Centre for Medium-Range Weather Forecasts, https://doi.org/10.21957/76cvnxi6d, 2003.

Matricardi, M., Chevallier, F., Kelly, G., and Thépaut, J.-N.: An improved general fast radiative transfer model for the assimilation of radiance observations, Quarterly Journal of the Royal Meteorological Society, 130, 153-173, https://doi.org/10.1256/qj.02.181, 2004.

https://doi.org/10.5194/egusphere-2025-5121
Preprint. Discussion started: 7 April 2026

Matricardi, M.: An inter-comparison of line-by-line radiative transfer models. European Centre for Medium-Range Weather Forecasts, 525, https://doi.org/10.21957/b3amji4k, 2007.

Matricardi, M.: The generation of RTTOV regression coefficients for IASI and AIRS using a new profile training set and a new line-by-line database, ECMWF Technical Memorandum, 564, https://doi.org/10.21957/59u3oc9es, 2008.

Matricardi, M.: The inclusion of aerosols and clouds in RTIASI, the ECMWF fast radiative transfer model for the infrared atmospheric sounding interferometer, ECMWF Technical Memorandum, 647, https://doi.org/10.21957/83f54g7h, 2008.

Matricardi, M. and McNally, T.: An assessment of the accuracy of the RTTOV fast radiative transfer model using IASI data, Atmospheric Chemistry and Physics, 8, 5079-5096, https://doi.org/10.5194/acp-8-5079-2008, 2008.

McMillin, L. M. and Fleming, H. E.: Atmospheric transmittance of an absorbing gas: a computationally fast and accurate transmittance model for absorbing gases with constant mixing ratios in inhomogeneous atmospheres, Appl. Opt., 15, 358-363, https://doi.org/10.1364/AO.15.000358, 1976.

McMillin, L. M., Crone, L. J., Goldberg, M. D., and Kleespies, T. J.: Atmospheric transmittance of an absorbing gas. 4. OPTRAN: a computationally fast and accurate transmittance model for absorbing gases with fixed and with variable mixing ratios at variable viewing angles, Appl. Opt., 34, 6269-6274, https://doi.org/10.1364/AO.34.006269, 1995.

Menzel, W. P., Schmit, T. J., Zhang, P., and Li, J.: Satellite-Based Atmospheric Infrared Sounder Development and Applications. Bulletin of the American Meteorological Society, 99(3), 1729–1738, 2018.

Rayer, P. J.: Fast transmittance model for satellite sounding, Appl. Optics, 34, 7387-7394, 1995.

Saunders, R., Matricardi, M., and Brunel, P.: An improved fast radiative transfer model for assimilation of satellite radiance observations, Quarterly Journal of the Royal Meteorological Society, 125, 1407-1425, https://doi.org/10.1002/qj.1999.49712555615, 1999.

Saunders, R., Hocking, J., Turner, E., Rayer, P., Rundle, D., Brunel, P., Vidot, J., Roquet, P., Matricardi, M., Geer, A., Bormann, N., and Lupu, C.: An update on the RTTOV fast radiative transfer model (currently at version 12), Geoscientific Model Development, 11, 2717-2737, https://doi.org/10.5194/gmd-11-2717-2018, 2018.

Schmit, T. J., Li, J., Lee, S. J., Li, Z., Dworak, R., Lee, Y. K., Bowlan, M., Gerth, J., Martin, G. D., and Straka, W.: Legacy atmospheric profiles and derived products from GOES-16: Validation and applications, Earth and Space Science, 6, 1730-1748, https://doi.org/10.1029/2019EA000729, 2019.

Wang, L., Tremblay, D., Zhang, B., and Han, Y.: Fast and accurate collocation of the visible infrared imaging radiometer suite measurements with cross-track infrared sounder, Remote Sensing, 8(1), 76, https://doi.org/10.3390/rs8010076, 2016.

Weng, F., Yu, X., Duan, Y., Yang, J., and Wang, J.: Advanced Radiative Transfer Modeling System (ARMS): A New-Generation Satellite Observation Operator Developed for Numerical Weather Prediction and Remote Sensing Applications, Advances in Atmospheric Sciences, 37, 131-136, https://doi.org/10.1007/s00376-019-9170-2, 2020.

Wu, C., Qi, C., Hu, X., Gu, M., Yang, T., Xu, H., Zhang, P., and Weng, F.: FY-3D HIRAS radiometric calibration and accuracy assessment, IEEE Trans. Geosci. Remote Sens., 58, 3965–3976, https://doi.org/10.1109/TGRS.2019.2959830, 2020.

Zeng, Z.-C., Clarisse, L., Franco, B., Clerbaux, C., Theys, N., Qi, C., Lee, L., Zhu, L., Hu, X., Gu, M., and Zhang, P.: Volcanic sulfur dioxide monitored from a constellation of FengYun hyperspectral infrared sounders in dawn-dusk, mid-morning, and afternoon sun-synchronous orbits. , Remote Sensing of Environment, Vol. 331, A115057, https://doi.org/10.1016/j.rse.2025.115057, 2025.

Zhang, P., Chen, L., Xian, D., and Xu, Z.: Recent Progress of Fengyun Meteorology Satellites, Chinese Journal of Space Science, 38(5), 788-796, https://doi.org/10.11728/cjss2018.05.788, 2018.

Zhang, P., Hu, X., Sun, L., Xu, N., Chen, L., Zhu, A., Lin, M., Lu, Q., Yang, Z., Yang, J., and Wang, J.: The On-Orbit Performance of FY-3E in an Early Morning Orbit. Bulletin of the American Meteorological Society, 105(1), E144-E175, https://doi.org/10.1175/BAMS-D-22-0045.1, 2024.

Zhou, M. Q., Y. P. Wang, C. Robert, X.-Y. Zhang, L. Zhang, Z. L. Deng, C. L. Qi, and P. C. Wang.: Global carbon monoxide column derived from HIRAS-II/FY-3F satellite observations. Adv. Atmos. Sci., 42(9), 1776−1782, https://doi.org/10.1007/s00376-025-5016-2, 2025.

Zhu, L., Bao, Y., Petropoulos, G. P., Zhang, P., Lu, F., Lu, Q., Wu, Y., and Xu, D. Temperature and Humidity Profiles Retrieval in a Plain Area from Fengyun-3D/HIRAS Sensor Using a 1D-VAR Assimilation Scheme. Remote Sensing, 12(3), 435. https://doi.org/10.3390/rs1203043, 2020.